PCCP

Accepted Manuscript

ROYAL SOCIETY OF CHEMISTRY

www.rsc.org/pccp

Oxygen reduction reaction activity and structural stability of Pt-Au nanoparticles prepared by arc-plasma deposition

Shuntaro Takahashi*, Hiroshi Chiba, Takashi Kato, Shota Endo, Takehiro Hayashi, Naoto Todoroki and Toshimasa Wadayama

Graduate School of Environmental Studies, Tohoku University, Aoba-ku, Aramaki Aoba 6-6-2, Sendai 980-8579, Japan

The oxygen reduction reaction (ORR) activity and durability of various Au_x/Pt_{100} nanoparticles (where x is the atomic ratio of Au against Pt) are evaluated herein. The samples were fabricated on a highly-oriented pyrolytic graphite substrate at 773 K through sequential arc-plasma depositions of Pt and Au. The electrochemical hydrogen adsorption charges (electrochemical surface area), particularly, the characteristic currents caused by corner and edge sites of the Pt nanoparticles decrease with increasing Au atomic ratio (x). In contrast, the specific ORR activities of the Au_x/Pt_{100} samples depended on the atomic ratios of Pt and Au: Au_{28}/Pt_{100} sample showed the highest specific activity among all the investigated samples (x = 0–42). As for ORR durability evaluated by applying potential cycles between 0.6 and 1.0 V in oxygen-saturated 0.1 M $HClO_4$, Au_{28}/Pt_{100} was the most durable sample against the electrochemical potential cycles. The results clearly showed that Au atoms located at coordinatively-unsaturated sites, *e.g.* at corners or edges of the Pt nanoparticles, can

improve the ORR durability by suppressing unsaturated-site-induced degradations of the Pt nanoparticles.

Tel:+81-22-795-7320;

*Corresponding author: shuntaro.takahashi.t3@dc.tohoku.ac.jp

Keywords: Oxygen reduction reaction catalysis; Platinum; Gold; Nanoparticles; Arc-plasma deposition

1. Introduction

Polymer electrolyte membrane fuel cells (PEMFCs) can be applied as low-environmental impact power sources for fuel cell vehicles (FCVs) and could therefore play a major role in a future carbon-free society.[1–3] At present, carbon-supported Pt (Pt/C) nanoparticles (NPs) are commonly used as oxygen reduction reaction (ORR) catalysts for the cathodes of PEMFCs. However under normal PEMFC operating conditions, the ORR activity of the Pt/C decreases as a result of the dissolution, aggregation, and detachment from the carbon support of the Pt NPs.[4–9] Therefore, a comprehensive understanding of the NP degradation process is indispensable to maximize the PEMFC lifetime. In particular, the electrochemical behaviour of Pt atoms located at the topmost surface of the NPs should be considered for discussing the electrochemical structural stability. Pt NPs generally comprise terrace, edge and corner sites, *e.g.* in cubo-octahedron NPs,[10] (111) and (100) facets form the terrace sites, whereas the corner and edge sites can be regarded as (111) facets separated by monatomic (110) steps such as (211) and (311).[10,11] The aforementioned Pt sites show the following trend in surface energy: (211) > (110) > (100) > (111).[12,13] This surface-energy trend is inversely proportional to the coordination number of the surface atoms. In other words, Pt atoms located at corner and edge sites have larger surface energies and lower coordination numbers compared with those located terrace sites. Consequently, Pt atoms located at coordinatively unsaturated sites determine the degradation behaviour of the Pt NPs through electrochemical oxidation and reduction under potential modulations, such as those observed under normal PEMFC operating conditions.[11,14,15]

Site blocking of the Pt NPs surface with Au atoms is expected to be an effective technique for the electrochemical stabilization of coordinatively unsaturated sites at Pt NP surfaces.[16,17] Based on first-principles simulations, Wei *et al.* proposed that the corrosion of Pt NPs at corner and edge sites can be hindered by framing using inert metals, *e.g.* Au.[18] They have explained that Au which has a much lower affinity toward oxygen and thereby could suppress the dissolution of Pt atoms if Au atoms located at corner and edge sites of Pt NPs. Deng *et al.* investigated the site selectivity of Au-atom segregations by using Monte Carlo simulations,[19] showing that the Au atoms segregate to available surface sites of Pt-Au NP and occupy the sites at corners and edges first, followed by the (100) and (111) facets. Furthermore, several groups studied the electrochemical stabilization of Pt NPs by Au clusters.[20,21] Adzic *et al.* deduced that the clusters preferentially locate at low-coordination facets of the Pt NPs, thus improving the electrochemical durability.[22] The published results indicate that Au atoms located at low-coordination sites of the Pt NPs could improve the electrochemical durability of the Pt/C catalysts. Because Au is inactive toward ORR, the addition of excess amounts of Au to the Pt/C is expected to reduce ORR activity.[23–25] Therefore, a precise control of the surface atomic ratios of Pt/Au NPs is a key to develop highly durable ORR catalysts.

Arc-plasma deposition (APD) is known the physical vapour deposition technique. Metal or alloy NPs can be fabricated by blowing ionized metal plasma,[3,26] which allows the preparation of the metal or alloy NPs on various substrates without any organic impurities. Because deposited amounts can be easily controlled by number of pulse repetitions and applied voltage, APD-fabricated NPs is expected to be suitable

for the evaluation of relation between structure and electro-catalytic behaviours not only for ORR but also other process, such as methanol oxidation reaction (MOR)[23,27] and electrochemical reduction of carbon dioxide (ERC).[28,29] In this study, NPs with various Pt/Au atomic ratios were prepared by sequential APD of Pt and Au on highly oriented pyrolytic graphite (HOPG) substrate under ultra-high-vacuum (UHV) conditions. Specific ORR activity as well as the electrochemical structural stability of the Pt/Au NPs was evaluated using the rotating disk electrode (RDE) method before and after applying several electrochemical potential cycles (PCs). Correlations between the Pt/Au atomic ratios and ORR properties of the UHV-APD-prepared Pt/Au NPs are discussed on the basis of the electrochemical properties and morphological changes induced by the PCs of Pt/Au NPs.

2. Experimental

Pt/Au NPs were prepared using two APD sources (ULVAC-RIKO ARL-300) under UHV (~10^{-8} Pa) conditions.[30] Highly-oriented pyrolytic graphite (HOPG, Optigraph) was used as the substrate. First, the surface of the HOPG was scraped in air using a scotch tape and cleaned by annealing at 773 K under UHV conditions. Then, NPs with various Pt/Au atomic ratios were prepared on the substrate by sequential depositions of Pt and Au using the respective arc-plasma sources (Fig. 1): applied voltages for Pt and Au APDs were fixed to 100 V and 70 V, respectively. The substrate temperature during the depositions was kept at 773 K to control the size distribution of the Pt NPs and activate the thermal segregation of the additionally deposited Au atoms on the Pt NP surfaces. A quartz-crystal microbalance coupled to the UHV-APD chamber was used to estimate the deposited amounts of Pt and Au. The Pt weight

(normalized to the HOPG geometric area) was fixed to approximately 0.7 μg/cm$^2_{HOPG}$. Subsequently, Au APD was conducted on the Pt NP/HOPG sample. The deposition weight of Au was controlled by pulse repetitions during the APD process. Hereafter, the prepared Pt-Au NPs will be denoted as Au_x/Pt_{100} NPs, where x is the atomic ratio of Au against the pre-deposited Pt on the substrate. The Au/Pt atomic ratios of the samples prepared in this study are summarized in table 1. The APD-prepared Pt-Au NPs/HOPG samples were transferred from the UHV-APD chamber to a conventional electrochemical cell that was set in an N_2-purged glove box without air exposure.[31] The electrochemical properties of the Pt-Au NPs/HOPG samples were evaluated in a three-electrode glass cell comprising the prepared samples as the working electrode, a Pt counter electrode and a reversible hydrogen electrode (RHE) as the reference electrode. Cyclic voltammetry (CV) studies were conducted in N_2-purged 0.1 M $HClO_4$. Linear-sweep voltammetry (LSV) experiments were conducted using the RDE method in O_2-saturated 0.1 M $HClO_4$. The specific ORR activities were evaluated from the kinetic controlled currents i_k at 0.9 V. These were estimated from Koutecky-Levich plots[32] and the hydrogen adsorption charges of the samples. Electrochemical degradation was investigated by square-wave potential cycling between 0.6 V (3 s) and 1.0 V (3 s) in O_2-saturated 0.1 M $HClO_4$ at room temperature (10000cycles, 10k-PCs). Sample morphologies of the Pt and Pt/Au NPs on the substrate before and after the cycles were observed by scanning tunnelling microscopy (STM, Bruker multi-mode V) in air. The NP distributions were calculated from the corresponding STM images using the ImageJ analysis software.[33] The Pt and Au/Pt NPs micro-structures prepared on amorphous carbon thin films were obtained by a high-angle annular dark-field scanning

transmission electron microscope (HAADF-STEM, JEOL JEM-ARM200F) equipped with energy dispersive X-ray (EDX) apparatus.

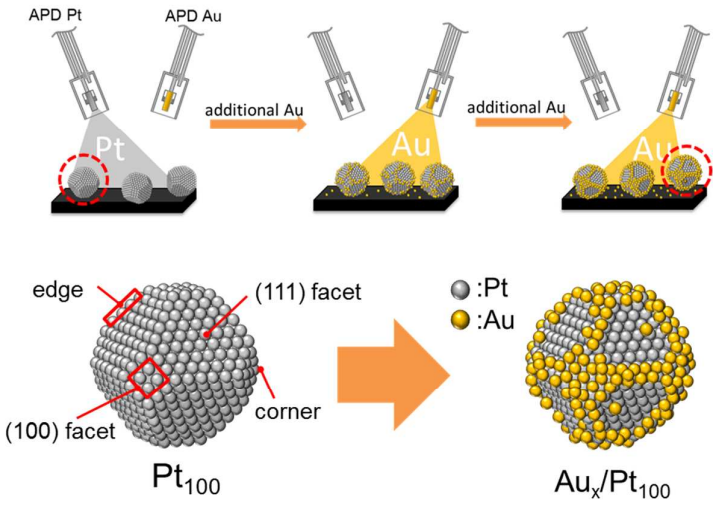

Fig. 1 Schematic image of sequential APD and structural models for APD-Pt_{100} and APD-Au_x/Pt_{100} NP.

Table 1 Compositions of the fabricated alloys estimated using a quartz-crystal microbalance

sample	Au [$\mu g/cm^2_{HOPG}$]	Pt [$\mu g/cm^2_{HOPG}$]
Pt_{100}	-	0.70
Au_7/Pt_{100}	0.05	0.70
Au_{14}/Pt_{100}	0.10	0.70
Au_{21}/Pt_{100}	0.15	0.70
Au_{28}/Pt_{100}	0.20	0.70
Au_{42}/Pt_{100}	0.30	0.70

3. Results and discussion

3-1. Specific ORR activity of the as-prepared Au_x/Pt_{100} samples

Fig. 2 presents (A) STM, (B) HAADF-STEM, (C) CV and (D) LSV results for the as-prepared Pt_{100} and Au_x/Pt_{100} samples. According to the STM images of Pt_{100} and Au_{42}/Pt_{100} NPs (fig. 2(A)), the average diameters of the particles can be estimated to be approximately 4 nm despite additional Au deposition. This indicates that additional Au APD does not significantly change the average diameters of the pre-deposited APD-Pt NPs under these conditions. Typical HAADF-STEM images of Pt_{100} and Au_{14}/Pt_{100} NPs were shown in Fig. 2(B). As for the later sample, ratios for center (blue square region) and surroundings (red) of the NP are analyzed by EDX. The Au:Pt ratios can be estimated to be 2:3 for the center region and 3:2 for the surroundings region, respectively. The CV curve of Pt_{100} (Fig. 2(C), left) exhibits an electrochemical charge that can be assigned to hydrogen adsorption (Q_{Hads}) in the potential region of approximately 0–0.4 V (vs. RHE.). The Q_{Hads} values obtained for the Au_x/Pt_{100} samples decrease with increasing x. Considering the inactivity of Au towards hydrogen adsorption,[34] Au-dependent decrease in Q_{Hads} suggest that additionally deposited Au atoms tend to locate on the surface of pre-deposited Pt NPs. This result is in good agreement with the Au/Pt atomic ratios estimated by the EDX and the surface segregation dependence of the Pt–Au alloy system,[35] in which the surface energy of Au (1.50 J/m^2) is lower than that of Pt (2.48 J/m^2).[36] Noticeably, the characteristic peaks observed around 0.13 V on the CV curves of the Pt NPs (resulting from hydrogen adsorption and desorption on corner or edge sites with (110)-like atomic arrangements)[34,37,38] decrease with increasing x. Because the corner or edge sites of

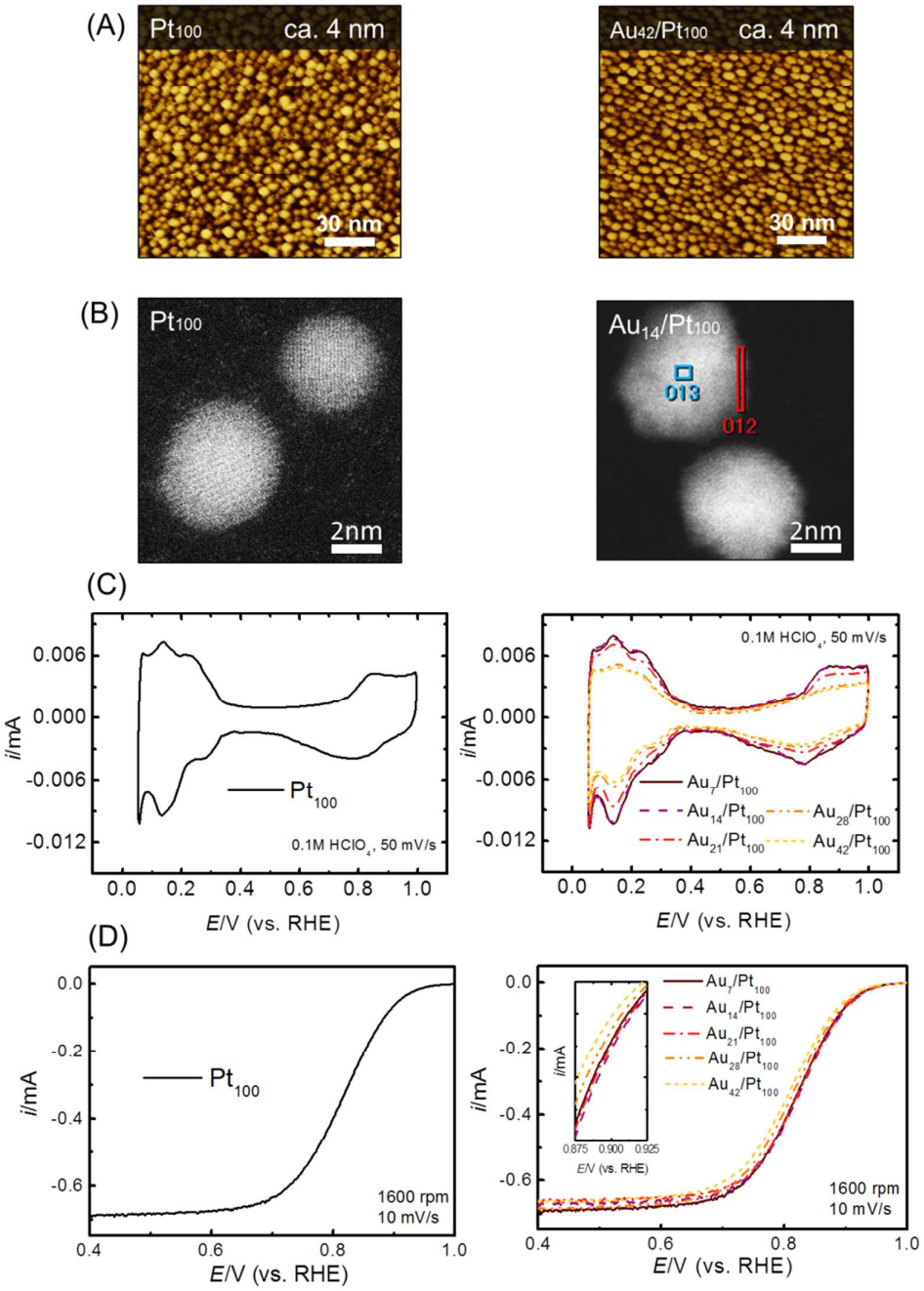

Fig. 2 (A) STM images (150 nm x 150 nm) of the Pt_{100} and Au_{42}/Pt_{100} NPs. (B) HAADF-STEM images (10 nm x10 nm) of the Pt_{100} and Au_{14}/Pt_{100} NPs. (C) CV curves and (D) LSV curves for the Pt_{100} and Au_x/Pt_{100} samples. The inset shows enlarged curves in the potential range between 0.875 and 0.925 V.

cubo-octahedron NPs comprise (111) facets separated by monatomic (110) steps, the decrease in the 0.13 V peaks should reflect preferential terminations of lower-coordinated sites of Pt NPs, such as corners and edges, by the additionally deposited Au atoms. As for the ORR activities of the samples, the LSV curves of the Au_x/Pt_{100} samples (Fig. 2(D)) shifted to lower potentials with increasing amounts of deposited Au, suggesting that the apparent ORR activities decrease with x. Generally, Au is inactive towards the ORR because of its filled d-band.[39] Therefore, the reduction in apparent ORR activity can be explained by a reduction in Q_{Hads} by the surface Au atoms. However, the surface-Au-dependent negative shift of the LSV curves does not exactly correspond to the Au-dependent reduction in Q_{Hads}.

For a detailed discussion of the Au-dependent CV and LSV changes, the specific ORR activities (j_k) were evaluated from the kinetic current (i_k) at 0.9 V using the corresponding electrochemical surface area (ECSA), which was estimated from the Q_{Hads} values in the potential region from 0.08 to 0.38 V. The ECSAs and specific ORR activities of the Au_x/Pt_{100} samples are summarized in Fig. 3. Typical values for the ECSA and specific activity of Pt_{100} sample were estimated to be approximately 0.12 cm^2 and 0.63 mA/cm^2, respectively. These values are presented by the dashed line. It can be seen that the specific ORR activity peaks at x = 28, *i.e.* Au_{28}/Pt_{100} sample is the most ORR-active sample among all the investigated Au_x/Pt_{100} samples. Although the Au atoms located on the HOPG substrate cannot be ruled out in the present sample fabrication condition, such a volcano-type specific ORR activity trend might correlate with the inhomogeneous distribution of Au atoms on the pre-deposited Pt NPs. It is well known that the relative surface ratios of various facets of the NPs depend on the particle

size.[10,19] In the case of octahedral NPs with an average diameter of 4 nm, the surface atoms that belong to corners, edges and (100) and (111) facets are approximately 1%, 20%, 14%, and 65%, respectively, of the total surface sites. If we assume that all the APD-Au atoms are located at the topmost surface of the Pt NPs forming a monolayer, the Au_7/Pt_{100} NPs is sufficient to cover the corners of 4-nm sized Pt NPs. Similarly, in the case of the Au_{28}/Pt_{100} NPs, the surface Au atoms are enough to cover the edges and (100) facets, in addition to the corners. In the case of the Au_{42}/Pt_{100} NPs, the amount of Au atoms corresponds to three-fourths of the surface Pt atoms, *i.e.* the Au atoms should influence all the surface Pt sites including the (111) facets. The surface Pt atoms located at the corner and edge sites of the Pt NPs are less ORR-active than the Pt atoms of the (111) and (100) facets as a result of poisoning by strongly bounding ORR intermediates.[11,40–43] Therefore, we deduce that additionally deposited Au atoms tend to locate at low-ORR-active site, *i.e.* as coordinatively unsaturated sites of the APD-Pt NPs. Thus, the specific ORR activity of the Au_x/Pt_{100} samples reveals the volcano-type trend shown in Fig. 3.

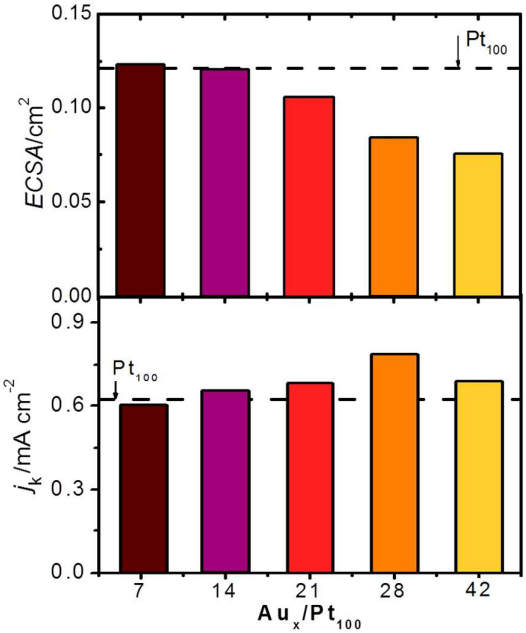

Fig. 3 Electrochemical surface area (ECSA: top) and initial specific activity (j_k: bottom) for Au_x/Pt_{100} samples.

3-2. Structural stability of the Pt/Au NPs upon applying PCs

Fig. 4 presents morphological (STM) and micro-structural (TEM) changes for (A) Pt_{100} and (B) Au_{28}/Pt_{100} NPs before and after applying the 10k-PCs. As for the Pt_{100} NPs (Fig. 4(A)), the average diameters estimated from the STM images increased from 4 nm for the as-prepared samples to 8 nm after 10k PCs. Typical HAADF-STEM images of the Pt_{100} NPs before and after applying 10k-PCs (bottom) suggest coalescence of Pt NPs. By contrast, STM and HAADF-STEM images of Au_{28}/Pt_{100} NPs (Fig. 4(B)) are nearly unchanged by applying 10k-PCs, indicating improvement in structural stability of Pt NPs by the Au atoms. Corresponding CV and LSV results for (A) Pt_{100} and (B) Au_{28}/Pt_{100} NPs were summarized in Fig. 5. Based on CV of Pt_{100} NPs

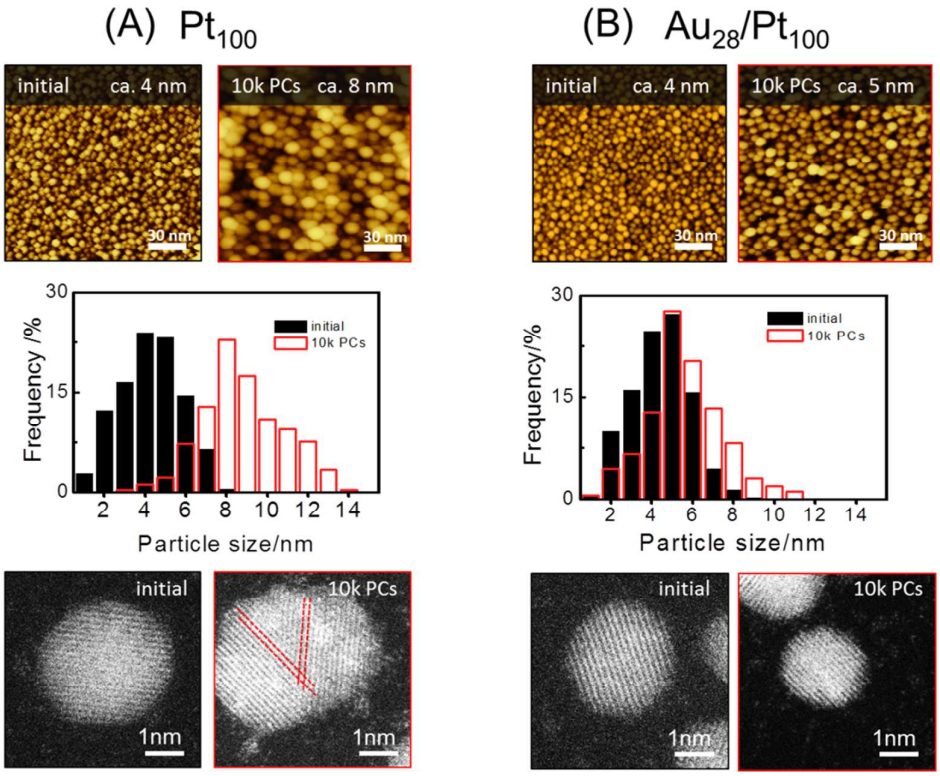

Fig. 4 STM images (150 nm x 150 nm) and typical HAADF-STEM images (5 nm x 5 nm) for (A) Pt_{100} and (B) Au_{28}/Pt_{100} NPs before (black) and after (red) applying 10k PCs.

(Fig. 5(A)), the ECSA after applying 10k PCs was estimated to be about 70% of the initial value. Furthermore, the LSV curves for Pt_{100} NPs shifted to negative potentials during the PCs, indicating ORR deactivation. In contrast, as shown in Fig. 5(B), the ECSA for Au_{28}/Pt_{100} NPs remained at 88% of its initial value. The reduction in ECSA can be directly related to a voltage loss in PEMFCs, *i.e.* to a reduction in the ORR activity.[41,42] Therefore, the morphological (STM and TEM), ECSA (CV) and ORR activity (LSV) changes induced by the PCs correspond well with each other and clearly indicate that the surface Au atoms, particularly those located at lower coordination sites of the Pt NPs, contribute to improvement in ORR durability. To determine the correlation between the ORR durability and Au deposition amounts (x), we investigated the changes in i_k values of Pt_{100} and Au_x/Pt_{100} samples during the PCs.

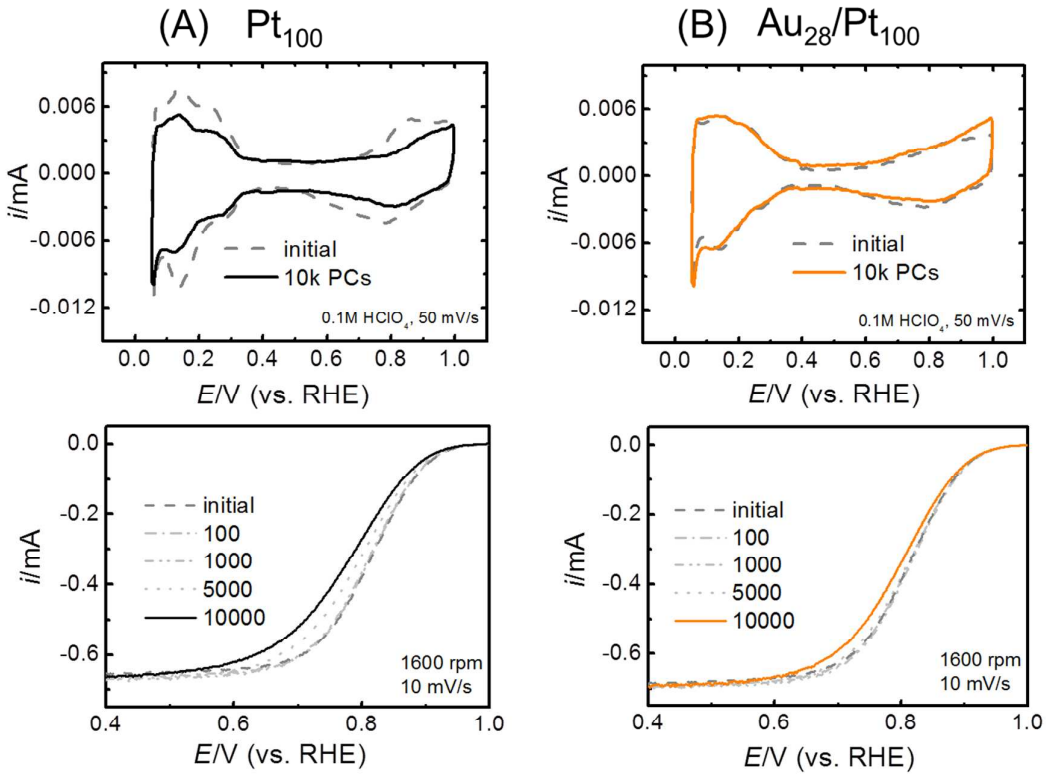

Fig. 5 CV and LSV curves for (A) Pt_{100} and (B) Au_{28}/Pt_{100} NPs recorded before (dotted line) and after (solid line) applying 10k PCs.

The results are shown in Fig. 6, where the mass activities of samples estimated based on i_k at 0.9 V are plotted. In the case of the Pt_{100} NPs (black closed circles), the activities steeply decreased with the number of PCs and the value after 10k PCs was about 60% of the initial value. This degradation is probably caused by dissolution and aggregation of Pt NPs during the PCs.[4,18,44] In literature, Pt dissolution preferentially occurs at larger surface energy sites which ORR intermediates easy adsorb,[18] *i.e.* coordinatively unsaturated sites. In contrast, the surface Au atoms can improve the ORR durability of the Au_x/Pt_{100} samples. All the Au_x/Pt_{100} samples remained their initial values up to 1k PCs. In particular, although the initial mass activity of the Au_{28}/Pt_{100} NPs (orange open diamond) was slightly lower than that of Pt_{100} NPs, the activities were almost constant until 5k PCs and maintained about 90% of the initial value even after the 10k PCs. The volcano-type ORR activity trend shown in Fig. 3 is probably caused by Au atoms located at coordinatively unsaturated sites of the APD-Pt NPs, with the

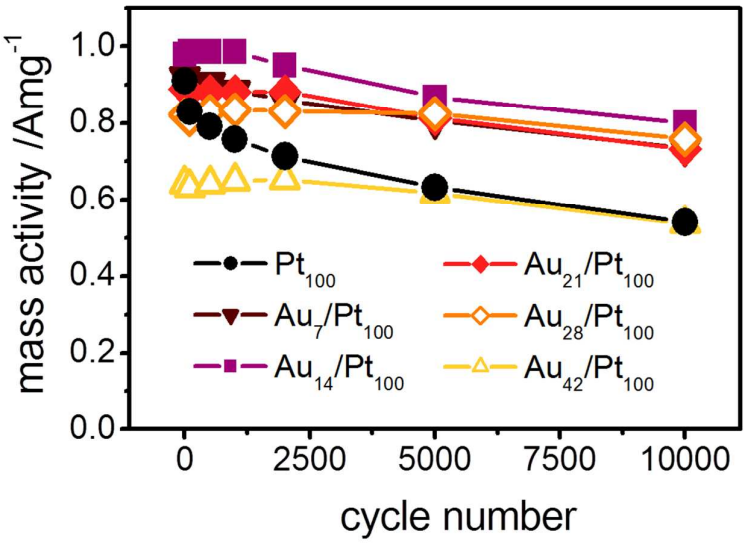

Fig. 6 Mass activity for Pt_{100} and Au_x/Pt_{100} samples during the PCs.

Au_{28}/Pt_{100} NPs showing the highest specific ORR activity. Therefore, the site-blocking effect of Au on coordinatively unsaturated sites of the Pt NPs should contribute to effectively suppress Pt NPs degradation, thus improving ORR durability of the Au_{28}/Pt_{100} NPs. The mass activities of Au_{42}/Pt_{100} NPs (yellow open triangle) are much lower than that of Au_{28}/Pt_{100} NPs, revealing that excess amounts of Au atoms particularly suppress ORR on the Pt NPs surface.

According to the literature,[4–9] Pt/C catalysts degrade by dissolution atoms, agglomeration and detachment from the carbon support of Pt NPs. The agglomeration of Pt NPs can be divided into two mechanisms: particle coalescence and electrochemical Ostwald ripening. Ostwald ripening proceeds through dissolution of the Pt atoms, mainly from smaller NPs followed by re-deposition on larger particles, *i.e.* it involves the growth of larger particles at the expense of the smaller ones.[4,45] Consequently, the particle-size distribution generally shifts to larger values, showing a tail toward larger particle sizes. The STM images of Pt_{100} NPs (Fig. 4(A), middle) clearly show that Pt NPs on the HOPG substrate remarkably aggregate through the PCs. Furthermore, particle-size distribution of the Pt_{100} NPs shifts to larger values by the PCs. The results clearly indicate that the degradation of such NPs can be explained by electrochemical Ostwald ripening. In contrast, the size distribution of the Au_{28}/Pt_{100} NPs (Fig. 4(B), middle) does not change that much, which suggests that the surface Au atoms located at lower coordination sites of the Pt NPs are stable during the PCs, suppressing the electrochemical Ostwald ripening process.

4. Summary

In this study, we fabricated Pt-Au NPs containing various atomic ratios (Au_x/Pt_{100} NPs) by sequential APD of the two components. The relations between the surface atomic ratios and the specific ORR activity and durability of the samples during PCs were investigated. The ECSAs of the Au_x/Pt_{100} samples decreased with increasing x. In particular, the electrochemical currents because of surface (110)-like sites of the Pt NPs decreased upon additional depositions of Au. Furthermore, the initial specific ORR activity of the Au_x/Pt_{100} samples revealed a volcano-type trend, with the Au_{28}/Pt_{100} NPs showing the highest specific activity among all the studies samples. Furthermore, the ORR durability of the Pt NPs was enhanced by surface Au atoms, with the Au_{28}/Pt_{100} being the most durable samples after the PCs. These results suggest that additionally deposited Au atoms are preferentially located at lower coordinated sites (such as corners and edges) of the Pt NPs, and that a sufficient amount of surface Au atoms can block the coordinatively unsaturated sites of the Pt NPs, thus enhancing their ORR durability.

Acknowledgement

This work was supported by New Energy and Industrial Technology Development Organization (NEDO) of Japan

References

1 J. K. Nørskov, J. Rossmeisl, A. Logadottir, L. Lindqvist, J. R. Kitchin, T. Bligaard and H. Jónsson, *J. Phys. Chem. B*, 2004, **108**, 17886–17892.

2 Z.-Y. Zhou, N. Tian, Z.-Z. Huang, D.-J. Chen and S.-G. Sun, *Faraday Discuss.*, 2008, **140**, 81–92; discussion 93–112.

3 E. Toyoda, R. Jinnouchi, T. Hatanaka, Y. Morimoto, K. Mitsuhara, A. Visikovskiy and Y. Kido, *J. Phys. Chem. C*, 2011, **115**, 21236–21240.

4 Y. Shao-Horn, W. C. Sheng, S. Chen, P. J. Ferreira, E. F. Holby and D. Morgan, *Top. Catal.*, 2007, **46**, 285–305.

5 J. Speder, A. Zana, I. Spanos, J. J. K. Kirkensgaard, K. Mortensen, M. Hanzlik and M. Arenz, *J. Power Sources*, 2014, **261**, 14–22.

6 H. Li, N. Cheng, Y. Zheng, X. Zhang, H. Lv, D. He, M. Pan, F. Kleitz, S. Z. Qiao and S. Mu, *Adv. Energy Mater.*, 2013, **3**, 1176–1179.

7 D. He, S. Mu and M. Pan, *Carbon N. Y.*, 2011, **49**, 82–88.

8 H. Lv and S. Mu, *Nanoscale*, 2014, **6**, 5063–74.

9 S. Yin, S. Mu, H. Lv, N. Cheng, M. Pan and Z. Fu, *Appl. Catal. B Environ.*, 2010, **93**, 233–240.

10 R. Van Hardeveld and F. Hartog, *Surf. Sci.*, 1969, 15, 189–230.

11 J. Greeley and J. Rossmeisl, *Zeitschrift für Phys. Chemie*, 2007, **221**, 1209–1220.

12 M. S. D. S.M. Foiles, M. I. Baskes, *Phys. Rev. B*, 1986, **33**.

13 Y.-N. Wen and J.-M. Zhang, *Solid State Commun.*, 2007, **144**, 163–167.

14 V. Komanicky, K. C. Chang, A. Menzel, N. M. Markovic, H. You, X. Wang and D. Myers, *J. Electrochem. Soc.*, 2006, **153**, B446–B451.

15 C. Burda, X. Chen, R. Narayanan and M. a El-Sayed, *Chem. Rev.*, 2005, 105, 1025–1102.

16 Y.-H. Fang and Z.-P. Liu, *J. Phys. Chem. C*, 2011, **115**, 17508–17515.

17 A. N. Kuznetsov, V. I. Zaikovskii, V. N. Parmon and E. R. Savinova, *Electrocatalysis*, 2012, **3**, 211–220.

18 G.-F. Wei and Z.-P. Liu, *Phys. Chem. Chem. Phys.*, 2013, **15**, 18555–18561.

19 L. Deng, W. Hu, H. Deng and S. Xiao, *J. Phys. Chem. C*, 2010, **114**, 11026–11032.

20 J. Zhang, K. Sasaki, E. Sutter and R. R. Adzic, *Science*, 2007, **315**, 220–222.

21 Y. Zhang, Q. Huang, Z. Zou, J. Yang, W. Vogel and H. Yang, *J. Phys. Chem. C*, 2010, **114**, 6860–6868.

22 K. Sasaki, H. Naohara, Y. Choi, Y. Cai, W.-F. Chen, P. Liu and R. R. Adzic, *Nat. Commun.*, 2012, 3, 1115.

23 J. Luo, L. Wang, D. Mott, P. N. Njoki, Y. Lin, T. He, Z. Xu, B. N. Wanjana, I.-I. S. Lim and C.-J. Zhong, *Adv. Mater.*, 2008, **20**, 4342–4347.

24 S. Senthil Kumar and K. L. N. Phani, *J. Power Sources*, 2009, **187**, 19–24.

25 A. Sarkar, J. B. Kerr and E. J. Cairns, *ChemPhysChem*, 2013, **14**, 2132–2142.

26 T. Ito, M. Kunimatsu, S. Kaneko, Y. Hirabayashi, M. Soga, Y. Agawa and K. Suzuki, *Talanta*, 2012, **99**, 865–870.

27 D. Mott, J. Luo, P. N. Njoki, Y. Lin, L. Wang and C.-J. Zhong, *Catal. Today*, 2007, **122**, 378–385.

28 W. Zhu, R. Michalsky, Ö. Metin, H. Lv, S. Guo, C. J. Wright, X. Sun, A. a Peterson and S. Sun, 2013, 2–5.

29 D. R. Kauffman, D. Alfonso, C. Matranga, H. Qian and R. Jin, *J. Am. Chem. Soc.*, 2012, **134**, 10237–43.

30 N. Todoroki, T. Kato, T. Hayashi, S. Takahashi and T. Wadayama, *ACS Catal.*, 2015, 2209–2212.

31 T. Wadayama, H. Yoshida, K. Ogawa, N. Todoroki, Y. Yamada, K. Miyamoto, Y. Iijima, T. Sugawara, K. Arihara, S. Sugawara and K. Shinohara, *J. Phys. Chem. C*, 2011, **115**, 18589–18596.

32 M. D. Maciá, J. M. Campiña, E. Herrero and J. M. Feliu, *J. Electroanal. Chem.*, 2004, **564**, 141–150.

33 C. a Schneider, W. S. Rasband and K. W. Eliceiri, *Nat. Methods*, 2012, **9**, 671–675.

34 Y. Iijima, T. Kondo, Y. Takahashi, Y. Bando, N. Todoroki and T. Wadayama, *J. Electrochem. Soc.*, 2013, **160**, F898–F904.

35 A. Ruban, H. Skriver and J. Nørskov, *Phys. Rev. B*, 1999, 59, 15990–16000.

36 S. Xiao, W. Hu, W. Luo, Y. Wu, X. Li and H. Deng, *Eur. Phys. J. B*, 2006, **54**, 479–484.

37 A. Kuzume, E. Herrero and J. M. Feliu, *J. Electroanal. Chem.*, 2007, **599**, 333–343.

38 Y. Iijima, Y. Takahashi, K. Matsumoto, T. Hayashi, N. Todoroki and T. Wadayama, *J. Electroanal. Chem.*, 2012, **685**, 79–85.

39 B. Hammer and J. K. Norskov, *Nature*, 1995, **376**, 238–240.

40 S. W. Lee, S. Chen, J. Suntivich, K. Sasaki, R. R. Adzic and Y. Shao-Horn, *J. Phys. Chem. Lett.*, 2010, **1**, 1316–1320.

41 G. a. Tritsaris, J. Greeley, J. Rossmeisl and J. K. Nørskov, *Catal. Letters*, 2011, **141**, 909–913.

42 F. J. Perez-Alonso, D. N. McCarthy, A. Nierhoff, P. Hernandez-Fernandez, C. Strebel, I. E. L. Stephens, J. H. Nielsen and I. Chorkendorff, *Angew. Chemie - Int. Ed.*, 2012, **51**, 4641–4643.

43 V. Tripković, I. Cerri, T. Bligaard and J. Rossmeisl, *Catal. Letters*, 2014, **144**, 380–388.

44 J. C. Meier, C. Galeano, I. Katsounaros, A. A. Topalov, A. Kostka, F. Schüth and K. J. J. Mayrhofer, *ACS Catal.*, 2012, **2**, 832–843.

45 K. Wettergren, F. F. Schweinberger, D. Deiana, C. J. Ridge, A. S. Crampton, M. D. Rötzer, T. W. Hansen, V. P. Zhdanov, U. Heiz and C. Langhammer, *Nano Lett.*, 2014, **14**, 5803–5809.